Parallel Computational Fluid Dynamics Conference (ParCFD2013)

High Performance Computing of the flow past a circular cylinder at critical and supercritical Reynolds numbers

Ivette Rodríguez[a,*], Oriol Lehmkuhl[a,b], Ricard Borrell[b], Leslye Paniagua[a], Carlos D. Pérez-Segarra[a]

[a]Technical University of Catalonia, ETSEIAT, Colom 11, 08222, Terrassa (Barcelona). Spain
[b]Termo Fluids, S.L., Avda. Jacquard, 97 1-E, 08222 Terrassa (Barcelona). Spain.

Abstract

It is well known that the flow past a circular cylinder at critical Reynolds number combines flow separation, turbulence transition, reattachment of the flow and further turbulent separation of the boundary layer. In the critical regime, the transition to turbulence in the boundary layer causes the delaying of the separation point and, an important reduction of the drag force on the cylinder surface known as the Drag Crisis. In this paper advanced turbulence simulations at Reynolds numbers in the range of 1.4×10^5-8.5×10^5 will be carried out by means of large-eddy simulations. Numerical simulations using unstructured grids up to 70 million of control volumes have been performed on Marenostrum Supercomputer. One of the major outcomes is shedding some light on the shear layer instabilities mechanisms and their role on the drag crisis phenomena.

1. Introduction

The flow past a circular cylinder is associated with different types of instabilities which involve the wake, the separated shear layers and the boundary layer. A comprehensive description of the flow phenomena at different Reynolds numbers (Re) can be found in [1]. It is well known that when Reynolds numbers approaches 2×10^5 the boundary layer undergoes a transition from laminar to turbulent regime. The range of Reynolds numbers up to $\sim 3.5 \times 10^5$ is characterised by a rapid decrease of the drag coefficient with the Reynolds numbers. Another feature which characterises this regime is the presence of asymmetric forces during the transition regime as reported experimentally [2, 3]. During this transition, the sepation point moves towards the rear end of the cylinder until it reaches a stationary point with a stable drag coefficient. This marks the transition from the critical to the supercritical regime [4].

This work aims at shed some light into the complex physics present at these critical and supercritical Reynolds numbers. To do this, large-eddy simulations of the flow at Reynolds numbers in the range of $Re = 1.4 \times 10^5$-8.5×10^5 are carried out. Solutions are compared to experimental measurements available in the literature. One of the major outcomes is to understand the physics that characterise both critical and supercritical regimes and the role of the turbulent transition in the boundary layer on the drag crisis phenomena.

---

* Corresponding author. Tel.: +34 937398192 ; fax: +34 937398020.
  E-mail address: cttc@cttc.upc.edu

---

2. Mathematical and numerical method

The spatially filtered Navier-Stokes equations can be written as,

$$\mathsf{M}\overline{\boldsymbol{u}} \quad = \quad \boldsymbol{0} \tag{1}$$

$$\frac{\partial \overline{\boldsymbol{u}}}{\partial t} + \mathsf{C}\left(\overline{\boldsymbol{u}}\right)\overline{\boldsymbol{u}} + \nu \mathsf{D}\overline{\boldsymbol{u}} + \rho^{-1}\mathsf{G}\overline{\boldsymbol{p}} \quad = \quad \mathsf{C}\left(\overline{\boldsymbol{u}}\right)\overline{\boldsymbol{u}} - \overline{\mathsf{C}\left(\boldsymbol{u}\right)\boldsymbol{u}}$$

$$\approx \quad -\mathcal{M}\mathcal{T}_{ij} \tag{2}$$

where $\overline{\boldsymbol{u}}$ and $\overline{\boldsymbol{p}}$ are the filtered velocity vector and pressure, respectively. ν is the kinematic viscosity and ρ the density. Convective and diffusive operators in the momentum equation for the velocity field are given by $\mathsf{C}\left(\overline{\boldsymbol{u}}\right) = \left(\overline{\boldsymbol{u}} \cdot \nabla\right)$, $\mathsf{D} = -\nabla^2$ respectively. Gradient and divergence (of a vector) operators are given by $\mathsf{G} = \nabla$ and $\mathsf{M} = \nabla\cdot$ respectively. The last term in equation 2 indicates some modelisation of the filtered non-linear convective term. $\mathcal{T}$ is the SGS stress tensor, which is defined as,

$$\mathcal{T}_{ij} = -2\nu_{sgs}\overline{S}_{ij} + (\mathcal{T}_{kk} : \boldsymbol{I})\boldsymbol{I}/3 \tag{3}$$

where $\overline{S}_{ij}$ is the large-scale rate-of-strain tensor, $\overline{S}_{ij} = \frac{1}{2}[\mathsf{G}(\overline{\boldsymbol{u}}) + \mathsf{G}^*(\overline{\boldsymbol{u}})]$, with G^* being the transpose of the gradient operator.

To close the formulation, a suitable expression for the subgrid-scale (SGS) viscosity must be introduced. LES studies have been performed using the wall-adapting local-eddy viscosity model within a variational multi-scale framework (VMS-WALE) [5, 6]. The variational multi-scale (VMS) approach was originally formulated for the Smagorinsky model by Hughes [6] is used here with the *small-small* strategy is used in conjunction with the wall-adapting eddy viscosity (WALE) model [5]. In VMS three classes of scales are considered: large, small and unresolved scales. If a second filter with filter length $\hat{\ell}$ is introduced (usually called test filter), a splitting of the scales can be performed, $f' = \overline{f} - \hat{f}$. For the large-scale parts of the resolved $\overline{\boldsymbol{u}}$ a general governing equation can be derived,

$$\frac{\partial \overline{\boldsymbol{u}}}{\partial t} + \mathsf{C}\left(\overline{\boldsymbol{u}}\right)\overline{\boldsymbol{u}} + \nu \mathsf{D}\overline{\boldsymbol{u}} + \rho^{-1}\Omega\mathsf{G}\overline{\boldsymbol{p}} = -\frac{\partial \widehat{\mathcal{T}}}{\partial x_j} - \frac{\partial \mathcal{T}'}{\partial x_j} \tag{4}$$

Neglecting the effect of unresolved scales in the large-scale equation ($\widehat{\mathcal{T}} \approx 0$), it is only necessary to model the $\mathcal{T}'$.

$$\mathcal{T}' \quad = \quad -2\nu_{sgs}\overline{S}_{ij}' + \frac{1}{3}\mathcal{T}'\delta_{ij} \tag{5}$$

$$\nu_{sgs} \quad = \quad (C_w^{vms}\ell)^2 \frac{(\overline{\Omega}_{ij}' : \overline{\Omega}_{ij}')^{\frac{3}{2}}}{(\overline{S}_{ij}' : \overline{S}_{ij}')^{\frac{5}{2}} + (\overline{\Omega}_{ij}' : \overline{\Omega}_{ij}')^{\frac{5}{4}}}$$

where $\overline{\Omega}_{ij}$ is the rate-of-rotation tensor. C_w^{vms} is the equivalent of the WALE coefficient for the *small-small* VMS approach. In our studies a value of $C_w = 0.325$ is used.

2.1. Numerical method

The governing equations have been discretised on a collocated unstructured grid arrangement by means of second-order spectro-consistent schemes. Such schemes are conservative, i.e. they preserve the symmetry properties of the continuous differential operators and, ensure both stability and conservation of the kinetic-energy balance even at high Reynolds numbers and with coarse grids. For the temporal discretisation of the momentum equation (2) a two-step linear explicit scheme on a fractional-step method has been used for the convective and diffusive terms [7], while for the pressure gradient term an implicit first-order scheme has been implemented. This methodology has been previously used with accurate results for solving the flow over bluff bodies with massive separation [8, 9].

2.2. Definition of the case. Geometry and mesh resolution.

We are considering here the flow past a circular cylinder at critical Reynolds numbers in the range of $Re = U_{ref} D/\nu = 1.4 \times 10^5 - 8.5 \times 10^5$. The Reynolds numbers is defined in terms of the free-stream velocity U_{ref} and the cylinder diameter D. The cases have been solved in a computational domain of dimensions $x \equiv [-16D, 16D]$; $y \equiv [-10D, 10D]$; $z \equiv [0, 0.5\pi D]$ in the stream-, cross- and span-wise directions, respectively, with a circular cylinder at $(0,0,0)$. As mentioned before, the governing equations are discretised on an unstructured mesh generated by the constant-step extrusion of a two-dimensional unstructured grid. Different grids up ~ 64 MCVs to have been used, depending on the Reynolds number (see Table 1). As we are not using any wall function in our formulation, the boundary layer should be well solved. Thus, in the near-wall region the mesh is highly refined. In fact, for Reynolds numbers $Re \geq 3.8 \times 10^5$, a prism layer is constructed around the cylinder surface as can be seen in Figure 1.

Table 1. Main parameters for the different computations. NCV_t total number of CVs; $N_{CV\ plane}$ number of CVs in the plane; N_{planes} number of planes in the span-wise direction

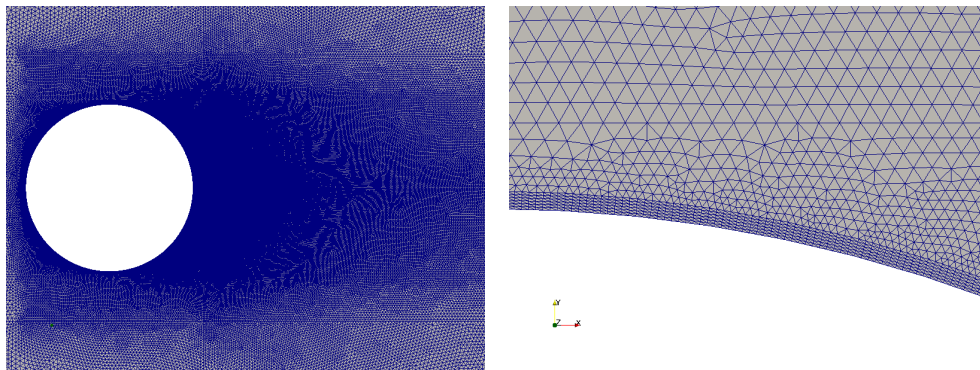| Re	NCV_t [MCVs]	$N_{CV\ plane}$	N_{planes}
1.44×10^5	38.4	299683	128
2.6×10^5	38.4	299683	128
3.8×10^5	48.6	379950	128
5.3×10^5	48.6	379950	128
7.2×10^5	64	500516	128
8.5×10^5	64	500516	128

Fig. 1. Detail of the computational 2D grid. (left) grid refinement around the cylinder. (right) Detail of the prism layer at the cylinder surface.

2.3. Boundary conditions

The boundary conditions at the inflow consist of a uniform velocity (u,v,w)=(1,0,0), slip conditions in the top and bottom boundaries of the domain, while at the outlet a pressure-based condition is used. At the cylinder surface, no-slip conditions are prescribed. As for the span-wise direction, periodic boundary conditions are imposed. As mentioned before, the governing equations are discretised on an unstructured mesh generated by the constant-step extrusion of a two-dimensional unstructured grid.

2.4. Computational details. Solving the Poisson equation.

Accordingly to the numerical method explained above, in order to respect the incompressibility constraint of the flow, a Poisson equations needs to be solved at each time-step to project the velocity field onto a divergence-free space. Due to the non-local nature of its solution, this elliptic system is the most time consuming and difficult to parallelize
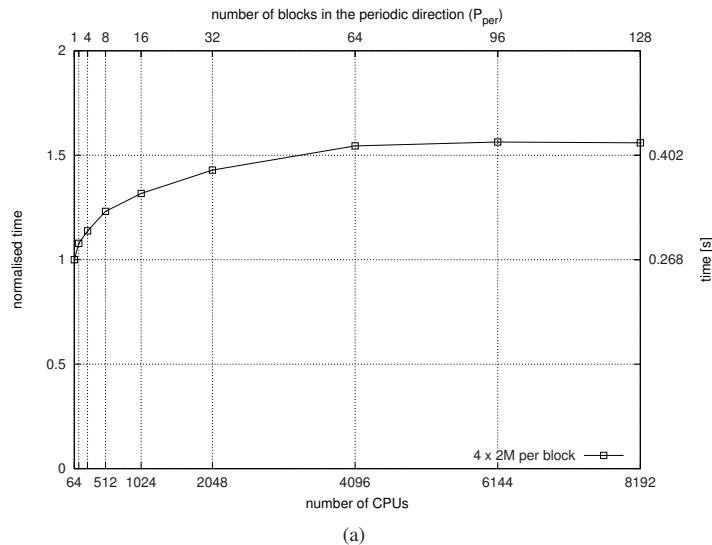
Fig. 2. Illustrative weak speed-up test for the direct Poisson solver, based in a FFT diagonalization and a Schur complement based decomposition

part of the code. Therefore, the optimization efforts are concentrated in this part of the algorithm, while the parallel performance of the rest of the code, which is based on explicit schemes, can be obtained much more effortless.

Since periodic boundary conditions are imposed in the span-wise direction, an FFT based method is being used decoupling the initial system into a set of two-dimensional subsystems, *i.e* diagonalizing the system in a Fourier space. Those subsystems, here referred to as frequency systems, are then solved by means of a direct Schur complement based (DSD) method. Therefore, a direct approach is composed - no iterative convergence scheme is required - which makes up a robust solution to the problem.

The parallelization is based on a geometric domain decomposition. Different partitions are employed for the FFT-based change-of-basis (from the *physical* to the *spectral* space and vice versa) and for the solution of the frequency systems. The former operation must be performed without partitioning the mesh in the span-wise direction - to avoid the parallelization of the FFT - whereas, for the latter, the number of processes to solve each frequency subsystem must be kept in the range of linear scalability of the DSD algorithm. Despite the additional transmissions of data between both partitions, this strategy benefits the scalability of the overall algorithm. The interested reader is referred to [10] for the full details.

The efficiency and scalability of this method was demonstrated for meshes with up to 10^9 million nodes engaging up to 8192 CPU in [10]. In Figure 2(a) is shown an illustrative weak speedup test performed in the MareNostrum supercomputer. The load per CPU is kept constant at around 125000 nodes varying the number of parallel process from 64 to 8192. The slowdown obtained when increasing the mesh and number of parallel processes 128 times is only of 1.5×. Its also remarkable that, in the now old fashioned MareNostrum II supercomputer, only 0.4 seconds where necessary to solve the 10^9 millions unknowns problem with 8192 CPU-cores.

3. Results

Figure 3 shows the isocontours of second invariant of the velocity gradient tensor (Q) coloured by the velocity magnitude at Reynolds numbers 1.44×10^5 and 5.3×10^5. While the lower Reynolds numbers exhibits a flow topology similar to that observed in the sub-critical regime, i.e. laminar flow separation at about ($\phi_s \sim 90°$) from the stagnation point and, transition to turbulence in the separated shear layers, at the higher Reynolds numbers the flow shows a narrow wake with the separation point moving towards the rear end of the cylinder ($\phi_s \geq 90°$).

The variation of the drag coefficient with the Reynolds number is plotted in 4(a) together with reference data from the literature. At these Reynolds numbers, the measured data of the drag coefficient present a large scattering. This is
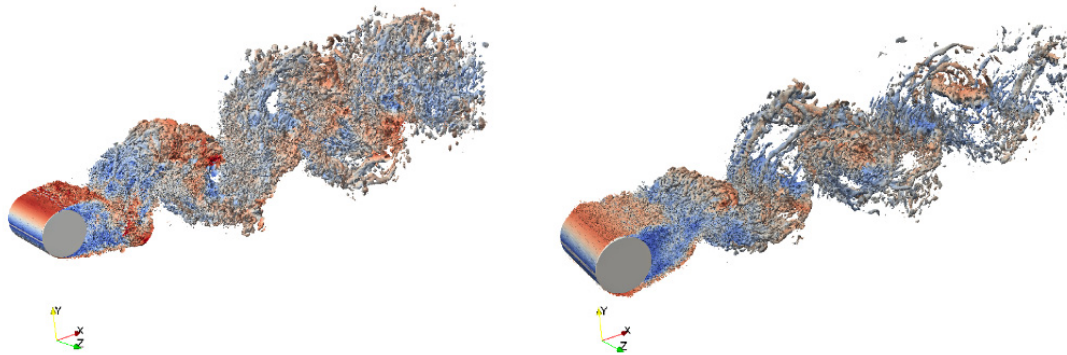
Fig. 3. Vortical structures represented by Q isocontours at different Reynolds numbers (left) $Re = 1.4 \times 10^5$; (right) $Re = 5.3 \times 10^5$.

due to the difficulties associated with the measurements; the flow is very sensitive to the different turbulence intensities, cylinder end conditions, surface roughness, blockage ratio (i.e. the ratio of the cylinder diametre to the wind tunnel height), etc. In spite of the large scattering in the reference data, results obtained with the present simulations show a fair agreement, being in the same range of the measured data.

In addition to the total drag coefficient, the pressure distribution at the cylinder at different Reynolds numbers is also shown in figure 4(b). As can be seen, at $Re = 1.44 \times 10^5$ it compares very well with that measured by Cantwell and Coles [15] at the same Reynolds number. As the Reynolds numbers increases, the pression distribution changes with a pronounced deacrese in the magnitude of the minimum pressure, and the position of this minima moving towards the rear end of the cylinder. At the same time the cylinder base pressure rises as also shown by Achenbach [11] in his study. This behaviour is characteristic of the critical regime.

One interesting feature observed in the present computations is the presence of asymmetric forces at the cylinder surface in the regime transition (in the present computations at $Re = 2.5 \times 10^5$). This behaviour, which causes large fluctuations in the cylinder forces and yields average lift $C_l > 0$, was also observed experimentally by Bearman [2] and Schewe [3]. As can be observed, at the larger Reynolds, forces at the cylinder recover their symmetry (see figure 4(b)) and the drag coefficient reaches its minimum value (see also figure 4(a)). In the final version of the manuscript, results of the different flow configurations observed at the different Reynolds numbers will be given, together with measurements of the local forces and characteristics frequencies of the flow.

Acknowledgements

References

[1] C H K Williamson. Vortex Dynamics in the Cylinder Wake. *Annual Review of Fluid Mechanics*, 28(1):477–539, 1996.
[2] PW Bearman. On vortex shedding from a circular cylinder in the critical Reynolds number regime. *J. Fluid Mech*, 37:577–585, 1969.
[3] G Schewe. On the force fluctuations acting on a circular cylinder in crossflow from subcritical up to transcritical Reynolds numbers. *Journal of Fluid Mechanics*, 133:265–285, 1983.
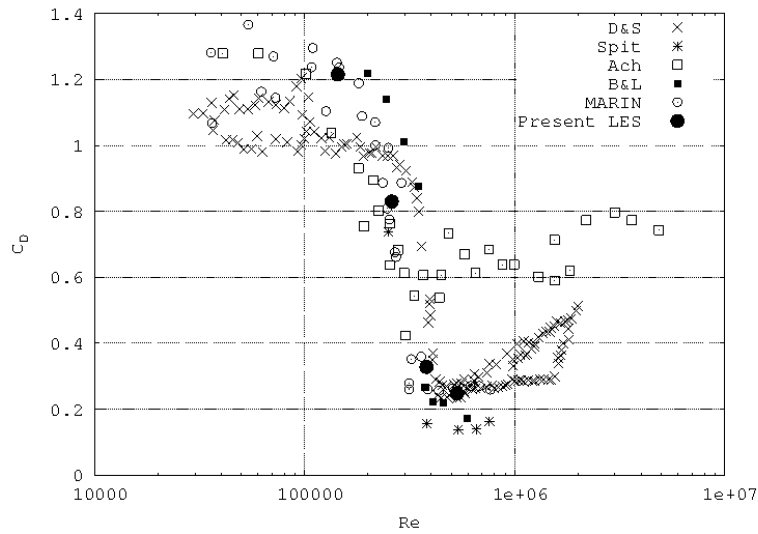
(a)
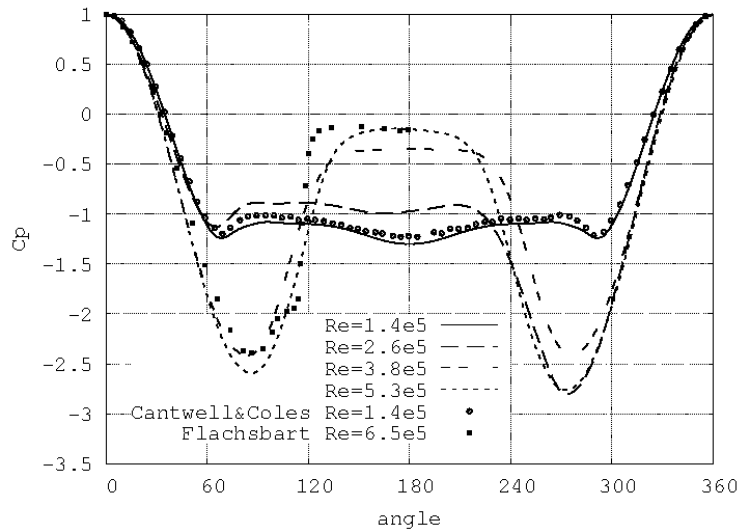
(b)

Fig. 4. (a)Variation of the drag coefficient with the Reynolds number. Comparison with the literature. (Solid dots) Present results, (squares) Achenbach [11], (solid squares) Bursnall and Loftin [12], (stars) Spitzer [13], (crosses) Delany and Sorensen [14]. (b) Asymmetries in the pressure distribution at critical Reynolds number.

[4] Anatol Roshko. Experiments on the flow past a circular cylinder at very high Reynolds number. *Journal of Fluid Mechanics*, 10(03):345, March 1960.

[5] F. Nicoud and F. Ducros. Subgrid-scale stress modelling based on the square of the velocity gradient tensor. *Flow, Turbulence and Combustion*, 62:183–200, 1999.

[6] T.J.R. Hughes, L. Mazzei, and K.E. Jansen. Large eddy simulation and the variational multiscale method. *Computing and Visualization in Science*, 3:47–59, 2000.

[7] F.X. Trias and O. Lehmkuhl. A self-adaptive strategy for the time integration of navier-stokes equations. *Numerical Heat Transfer. Part B*, 60(2):116–134, 2011.

[8] I. Rodríguez, R. Borrell, O. Lehmkuhl, C.D. Pérez-Segarra, and A. Oliva. Direct Numerical Simulation of the Flow Over a Sphere at Re = 3700. *Journal of Fluid Mechanics*, 679:263–287, 2011.

[9] I. Rodríguez, O. Lehmkuhl, R. Borrell, and A. Oliva. Flow dynamics in the wake of a sphere at sub-critical Reynolds numbers. *Computers & Fluids*, 2012.

[10] R. Borrell, O. Lehmkuhl, F.X. Trias, and A. Oliva. Parallel direct poisson solver for discretisations with one fourier diagonalisable direction. *Computational Physics*, 230(12):4723–4741, 2011.

[11] E. Achenbach. Distribution of local pressure and slin friction around a circular cylinder in cross-flow up to Re=5e6. *J. Fluid Mech*, 34:625–639, 1968.

[12] WJ Bursnall and L.K. Jr Loftin. Experimental investigation of the pressure distribution about a yawed circular cylinder in the critical Reynolds number range. Technical Report NACA TN2463, NACA, 1951.

[13] R.E. Spitzer. *Measurements of unsteady pressures and wake fluctuations for flow over a cylinder at supercritical Reynolds number*. PhD thesis, California Institute of Technology, 1964.

[14] NK Delany and NE Sorensen. Low-speed drag of cylinders of various shapes. Technical Report NACA TN3038, NACA, 1953.

[15] Brian Cantwell and Donald Coles. An experimental study of entrainment and transport in the turbulent near wake of a circular cylinder. *Journal of Fluid Mechanics*, 136:321–374, 1983.